# A Multifunctional Complex Droop Control Scheme for Dynamic Power Management in Hybrid DC Microgrids

Ali Hosseinipour[a], Javad Khazaei[a]

[a]*Department of Electrical and Computer Engineering at Lehigh University,*

## Abstract

It is crucial for hybrid DC microgrids (MGs) to employ power management strategies that take into account the dynamic characteristics of all energy sources in the system. This paper proposes a novel complex droop control (CDC) for voltage control units in hybrid DC MGs, which enables flexible power management by providing the capability to adjust steady-state and dynamic power sharing in addition to damping provision by leveraging a multifunctional droop function. To accurately tune the splitting frequencies that determine the performance of dynamic power sharing, a novel design procedure based on a reduced-order DC MG model is proposed. To gain insight into the dominant oscillatory modes and the impact of the proposed control on the stability of the hybrid DC MG, a system-level small-signal analysis is also conducted. Offline and real-time simulations of the hybrid DC MG subjected to pulsed-power load variations reveal that the CDC can effectively share dynamic power, while improving voltage regulation and damping.

*Keywords:* hybrid DC microgrid, droop control, small-signal modeling, dynamic power sharing

## 1. Introduction

DC distribution technology provides various advantages in applications such as railways [1], shipboards [2], electric vehicle charging stations [3], as well as data centers and wind collection grids [4]. Particularly, DC microgrids (MGs) benefit from easier connection of renewable energy sources and storage, which are inherently DC, elimination of reactive power control and phase synchronization, reduced bulk, and improved fuel economy and power quality compared with their AC counterparts [5].

Despite the above-mentioned advantages, challenges arise in the design of DC MGs with respect to specified power sharing control and stability preservation of mixed-source, also known as hybrid MGs [6]. There have been a multitude of efforts on steady-state power sharing control in hybrid DC MGs. Droop control is the most widely used method for power sharing between multiple energy sources in MGs [7]. Variations of droop control for state of charge balancing of battery energy storage systems (BESSs) have been reported in [8] and [9]. Supervisory control is also developed for improvement of primary level controllers and optimized power management of DC MGs in the form of centralized [10, 11] and distributed [12, 13] controllers.

Due to the heterogeneous nature of sources in hybrid MGs, dynamic power sharing should also be taken into account in the design stage of these systems. Hybrid energy storage systems provide flexibility to take advantage of high energy density and high power density energy storage technologies at the same time [14]. The most prevalent frequency-based power management is the filter-based method, where low- and high-pass filters are inserted within the control loops of the high energy density and high power density energy storage devices, respectively [15, 16, 17]. However, this method can lead to leakage current for high power density storage devices such as supercapacitors (SCs) as the result of a limited gain for dc and low-frequency error signals [18]. Moreover, adjustment of the filter parameters requires the retuning of inner converter controllers. Model predictive control (MPC) is utilized for power management of hybrid DC MGs in [19, 20, 21]. However, these methods are still reliant on filters to allocate the transient power and also suffer from a high computational load as the number of heterogeneous sources increase.

Dynamic droop control methods have been proposed for frequency-based power management of hybrid energy storage systems in [22, 23, 24]. With droop-based methods, the adjustment of frequency divisions is decoupled from the design of voltage and current controllers, providing flexibility for independent tuning of the controllers and the frequency-based power decoupling. However, the application of methods proposed in [22, 23, 24] is limited to DC MGs with two types of heterogeneous sources. Another droop-based dynamic power sharing approach is also proposed in [25], which only considers power sharing between synchronous generators (SGs). Recently, [26] has proposed a droop-based dynamic power sharing strategy that can be extended to multiple heterogeneous sources and enables dividing the frequency domain into multiple regions for power sharing purposes. However, in this approach, BESSs can only respond to medium-frequency variations of power with no

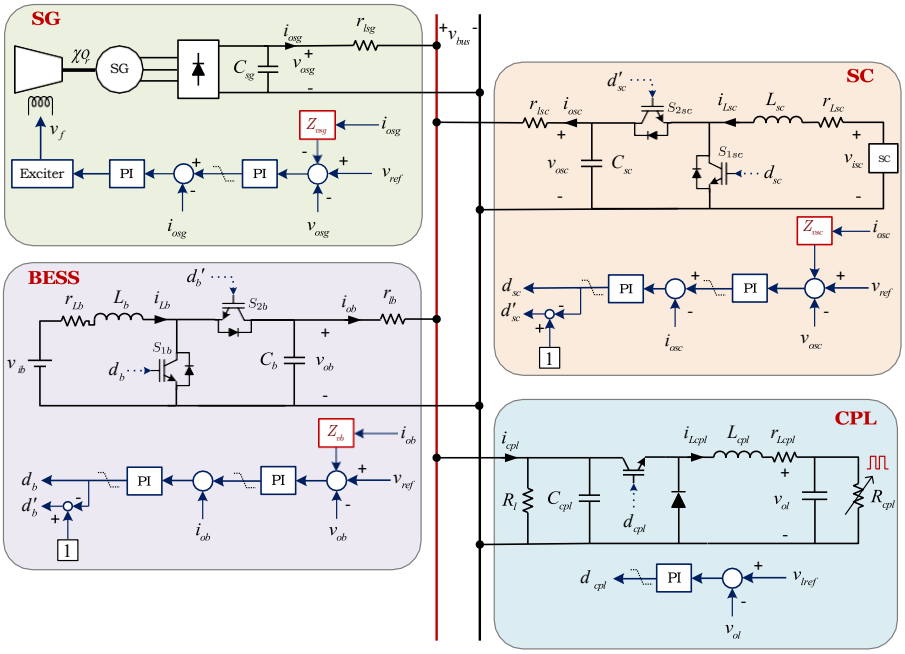


Figure 1: Implementation of the proposed control scheme for a hybrid DC MG.

contribution to steady-state voltage regulation. This leads to the negligence of back-up power capability of BESSs and the requirement for more back-up power from SGs. Moreover, a simplified equivalent model that is only valid at low frequencies is used to design the droop gains, which leads to significant error in dynamic power sharing adjustment. The study also lacks a system-level stability analysis to assess the impact of droop gains. To address the aforementioned knowledge gap, this study proposes a complex droop control (CDC) scheme for a hybrid DC MG with multiple voltage control units, which provides multiple functions for both static and dynamic power sharing adjustment as well as damping enhancement. Table 1 compares the proposed method with the state-of-the-art dynamic power management methods for hybrid DC MGs. The main contributions of the paper include:

- The proposed multifunctional CDC has the capability to be applied to multiple heterogeneous sources in hybrid DC MGs. The CDC is able to adjust static and dynamic power sharing and provide damping function in a universal droop control setting.

- Detailed design of droop gains is discussed based on a reduced-order

Table 1: State-of-the-art research on dynamic power management in hybrid DC MGs

| Reference | Method | Multiple-source capability | Stability analysis | Improved damping |
|---|---|---|---|---|
| [15] | Filter-based | ✗ | ✗ | ✗ |
| [16] | Filter-based | ✗ | ✓ | ✗ |
| [19] | MPC+filter | ✗ | ✗ | ✗ |
| [20, 21] | MPC+filter | ✗ | ✓ | ✗ |
| [22, 23] | Droop-based | ✗ | ✓ | ✗ |
| [24] | Droop-based | ✗ | ✗ | ✗ |
| [25] | Droop-based | ✗ | ✗ | ✗ |
| [26] | Droop-based | ✓ | ✗ | ✗ |
| Proposed | Droop-based | ✓ | ✓ | ✓ |

model of the hybrid DC MG, which achieves accurate frequency divisions for voltage control units response and improves on the state-of-the-art droop-based dynamic power management designs that lead to high errors in the frequency domain partitioning.

- A comprehensive small-signal stability analysis is conducted to gain insight into the dominant oscillatory modes of the hybrid DC MG and the impact of the proposed control on the identified modes. The proposed method enhances the damping of the high-frequency mode of the hybrid DC MG without the need to oversize the BESS and SC.

The rest of the paper is organized as follows. Section 2 introduces the studied hybrid DC MG and the proposed control. In Section 3, the design of the CDC is discussed. Section 4 provides an evaluation of the system dominant oscillatory modes and the impact of control parameters on the system small-signal stability. Section 6 presents simulation case studies. The paper is concluded with a summary of findings in Section 7.

## 2. Hybrid DC MG Configuration and Proposed Dynamic Power Management

### *2.1. System Configuration*

The configuration of the study hybrid DC MG is depicted in Fig. 1. The SG is interfaced with a rectifier unit and provides the majority of power to

balance the generation and demand. The BESS and SC are connected to the main DC bus through bidirectional DC-DC converters that enable charging and discharging power flow. The load bank consists of a resistive and a converter-based electronic load, which exhibits constant power load (CPL) behavior [27]. All the three types of sources are voltage control units that are required to share power in order to maintain a stable voltage at the main bus.

### *2.2. Proposed CDC Scheme*

The proposed droop control scheme is designed to achieve dynamic power sharing so that the SG exclusively responds to low-frequency fluctuations of power, the BESS responds to medium-frequency as well as steady-state components of power, and the SC solely picks up high-frequency power transients in the system. To this end, a universal CDC is proposed for voltage control units in a hybrid DC MG that can be represented by:

$$v_{ox} = v_{ref} - Z_{cdc} i_{ox} \tag{1}$$

where $x \in \{b, sc, sg\}$. $v_{ox}$ and $i_{ox}$ are the output voltage and output current of the voltage control unit, respectively. The CDC droop gain is decided by

$$Z_{cdc}(s) = R_v || (r_v + \frac{1}{C_v s}) = \frac{R_v(r_v C_v s + 1)}{C_v(r_v + R_v)s + 1} \tag{2}$$

where $R_v$ is the virtual resistance, $r_v$ is the virtual damping resistance, and $C_v$ is the virtual capacitance.

From (2), it can be seen that the CDC gain is the equivalent parallel impedance of the series $r_v$&$C_v$ and $R_v$, which results in a general first-order filter transfer function that can be tuned to achieve desired filtering performance. The multi-variable CDC in (2) is deemed universal in that the droop gain of all voltage control units are special cases of $Z_{cdc}$. In order to achieve the desired dynamic power sharing between the heterogeneous power sources, the individual droop gains are selected as

$$Z_{vsg}(s) = R_{vsg} \tag{3}$$

$$Z_{vb}(s) = R_{vb} || (r_{db} + \frac{1}{C_{vb} s}) = \frac{R_{vb}(r_{db} C_{vb} s + 1)}{C_{vb}(r_{db} + R_{vb})s + 1} \tag{4}$$

$$Z_{vsc}(s) = r_{dsc} + \frac{1}{C_{vsc} s} = \frac{r_{dsc} C_{vsc} s + 1}{C_{vsc} s} \tag{5}$$

where $Z_{vsg}$, $Z_{vb}$, and $Z_{vsc}$ are the droop gains for the SG, BESS, and SC, respectively. $R_{vsg}$ and $R_{vb}$ are virtual resistances for the SG and BESS, respectively. $C_{vb}$ and $C_{vsc}$ also represent virtual capacitances for the BESS and SC, respectively. Damping resistances for the BESS and SC are denoted by $r_{db}$ and $r_{dsc}$, respectively.

Since the response of voltage and current controllers are much faster than the droop control, the simplified equivalent circuit of the system can be illustrated as in Fig. 3 [26], where the line impedances are represented by $r_{lx}$, with $x \in \{b, sc, sg\}$. It will be shown later that the damping resistances ($r_{db}$ and $r_{dsc}$) generally possess small values and thus will have minimum effect on the dynamic power sharing performance. Neglecting the effect of these damping resistances and applying the current divider rule, the output currents of the source-side converters in Fig. 3 can be obtained as

$$i_{osg} = G_{fsg}(s) i_{cpl} \tag{6}$$

$$i_{ob} = G_{fb}(s) i_{cpl} \tag{7}$$

$$i_{osc} = G_{fsc}(s) i_{cpl} \tag{8}$$

where $i_{osg}$, $i_{ob}$, $i_{osc}$ are the output currents of the SG, BESS, and SC converters, respectively; $i_{cpl}$ is the aggregated load bank current. By applying the current division rule to the circuit of Fig. 3, we obtain

$$G_{fsg}(s) = \frac{Z_T}{Z_{vsg}} = \frac{R_{vb}}{R_{vb} + R_{vsg}[1 + (R_{vb}C_{vb} + R_{vb}C_{vsc})s]} \tag{9}$$

$$G_{fb}(s) = \frac{Z_T}{Z_{vb}} = \frac{R_{vsg}(1 + R_{vb}C_{vb}s)}{R_{vb} + R_{vsg}[1 + (R_{vb}C_{vb} + R_{vb}C_{vsc})s]} \tag{10}$$

$$G_{fsc}(s) = \frac{Z_T}{Z_{vsc}} = \frac{R_{vsg}R_{vb}C_{vsc}s}{R_{vb} + R_{vsg}[1 + (R_{vb}C_{vb} + R_{vb}C_{vsc})s]} \tag{11}$$

where $Z_T = (Z_{vsg}(s)^{-1} + Z_{vb}(s)^{-1} + Z_{vsc}(s)^{-1})^{-1}$.

As can can be inferred from (9)-(11) and shown in Fig. 2, the SG responds to low-pass-filtered components of the load, while the SC picks up the high-pass-filtered load current. On the other hand, the BESS current consists of both low- and high-pass-filtered components of the load. The detailed design of the CDC gains will be discussed in Section 3 to achieve the desired power splitting in frequency domain.

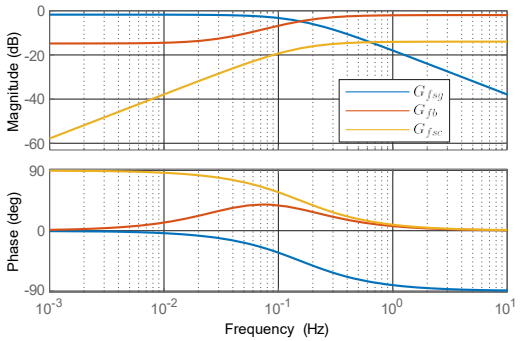


Figure 2: Filtering performance of the CDC.

Table 2: Operating Modes of the hybrid DC MG

| Parameter | Mode 1 | Mode 2 |
|---|---|---|
| System Loading | $P_{gmin} < P_l < P_{gmax}$ | $P_{gmin} - P_{cbmax} < P_l < P_{gmin}$ |
| SG Control Mode | Droop | Constant Current Control |
| BESS Control Mode | Droop (Discharging) | Droop (Charging) |
| SC Control Mode | Droop | Droop |

### *2.3. Modeling and control of sources and loads*

Fig. 1 shows the implementation of the proposed control scheme. The operating modes of the hybrid DC MG based on different loading scenarios are defined as in Table 2. It is recommended for the SG to always operate with a high utilization factor due to the fact that in low-load conditions the specific fuel consumption of the SG driving engine increases [7]. In the proposed method, the SG is controlled with the droop control. However, when the load power drops below the 60% of the SG rated power, the SG is controlled at a constant output current corresponding to the 60% of its nominal power. It should be noted that the system load is assumed to be between $P_{gmin} - P_{cbmax}$ and $P_{gmax}$, where $P_{gmin}$ is 60% of the SG nominal power, $P_{gmax}$ is the rated power of the SG, and $P_{cbmax}$ is the maximum charging current of the BESS. This makes the BESS always operate in the droop control mode and prevents it from operating in the constant current charging or discharging mode realized by its current saturation unit. Furthermore, the state-of-charge of the BESS and SC is assumed to be within the permissible limits, and thus they're not required to disconnect from the system, which is a requirement in case the storage units are overly charged or discharged.

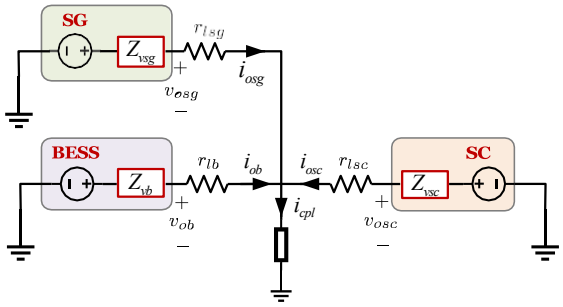


Figure 3: Simplified equivalent circuit of the hybrid DC MG with the proposed CDC [26].

### *2.3.1. BESS and SC control*

Referring to Fig. 1, both the BESS and SC converters employ the cascade voltage and current control structure, with the steady-state droop gain of the BESS, $R_{vb}$, determined by

$$R_{vb} = \frac{\Delta V_{obmax}}{I_{obmax}} \tag{12}$$

where $\Delta V_{obmax}$ is the maximum permissible steady-state variation of the converter output voltage and $I_{omax}$ is the maximum output current rating of the BESS.

The BESS/SC converter with the topology shown in Fig. 1, operates either in the boost or buck mode to enable bidirectional power flow. In the boost mode, the converter dynamics are represented by

$$\frac{d}{dt}\begin{bmatrix} i_{Lx} \\ v_{ox} \end{bmatrix} = \begin{bmatrix} 1/L_x & -r_{Lx}/L_x & (s_{1x}-1)/L_x & 0 \\ 0 & (1-s_{1x})/C_x & 0 & -1 \end{bmatrix} \begin{bmatrix} v_{ix} \\ i_{Lx} \\ v_x \\ i_{ox} \end{bmatrix} \tag{13}$$

where $x \in \{b, sc\}$. $v_{ix}$ is the input voltage, $r_{Lx}$ is the equivalent series resistance of the inductor, $L_x$ is the input inductance, $i_{Lx}$ is the inductor current, and $C_x$ is the output capacitance. $s_{1x}$ is one when switch $S_{1x}$ is conducting, and is zero when switch $S_{1x}$ is off.

In the buck mode, the converter dynamics are governed by

$$\frac{d}{dt}\begin{bmatrix} i_{Lx} \\ v_{ox} \end{bmatrix} = \begin{bmatrix} 1/L_x & -r_{Lx}/L_x & -s_{2x}/L_x & 0 \\ 0 & s_{2x}/C_x & 0 & -1/C_x \end{bmatrix} \begin{bmatrix} v_{ix} \\ i_{Lx} \\ v_{ox} \\ i_{ox} \end{bmatrix} \tag{14}$$

where $s_{2x}$ is one when $S_{2x}$ is conducting, and is zero when $S_{2x}$ is off.

Applying the state-space averaging technique [28], the averaged model of the BESS/SC bidirectional converter can be obtained as

$$\frac{d}{dt}\begin{bmatrix} \bar{i}_{Lx} \\ \bar{v}_{ox} \end{bmatrix} = \begin{bmatrix} 1/L_x & -r_{Lx}/L_x & -1/L_x & 1/L_x & 0 & 0 \\ 0 & 1/C_x & 0 & 0 & -1/C_x & -1/C_x \end{bmatrix} \begin{bmatrix} \bar{v}_{ix} \\ \bar{i}_{Lx} \\ \bar{v}_{ox} \\ \bar{d}_x \bar{v}_{ox} \\ \bar{d}_x \bar{i}_{Lx} \\ \bar{i}_{ox} \end{bmatrix} \tag{15}$$

The parameters with the bar sign represent the averaged values, with $\bar{d}_x$ denoting the average duty cycle of switch $S_{1x}$.

By linearizing (15), the closed-loop small-signal block diagram of the BESS and SC converters can be derived as in Fig. 4, where $G_{vx}(s)$ is the voltage controller transfer function, $G_{ix}(s)$ is the current controller transfer function, and $Z_{vx}(s)$ is the droop gain for $x \in \{b, sc\}$. The converter open-loop transfer functions representing its power stage dynamics are given by

$$Z_{outx}(s) = \frac{-\tilde{v}_{ox}}{\tilde{i}_{ox}}\Big|_{\tilde{v}_{ix}, \tilde{d}_x = 0} = \frac{L_x s + r_{Lx}}{L_x C_x s^2 + r_{Lx} C_x s + (1 - D_x)^2} \tag{16}$$

$$G_{vdx}(s) = \frac{\tilde{v}_{ox}}{\tilde{d}_x}\Big|_{\tilde{v}_{ix}, \tilde{i}_{ox} = 0} = \frac{-L_x I_{Lx} s - r_{Lx} I_{Lx} + V_{ix}}{L_x C_x s^2 + r_{Lx} C_x s + (1 - D_x)^2} \tag{17}$$

$$G_{idx}(s) = \frac{\tilde{i}_{Lx}}{\tilde{d}_x}\Big|_{\tilde{v}_{ix}, \tilde{i}_{ox} = 0} = \frac{C_x V_{ox} s + I_{Lx}(1 - D_x)}{L_x C_x s^2 + r_{Lx} C_x s + (1 - D_x)^2} \tag{18}$$

$$A_{iox}(s) = \frac{-\tilde{i}_{Lx}}{\tilde{i}_{ox}}\Big|_{\tilde{v}_{ix}, \tilde{d}_x = 0} = \frac{-(1 - D_x)}{L_x C_x s^2 + r_{Lx} C_x s + (1 - D_x)^2} \tag{19}$$

where $x \in \{b, sc\}$. $I_{Lx}$, $V_{ox}$, and $D_x$ represent the steady-state values of the inductor current, output voltage, and duty cycle at the linearization point,

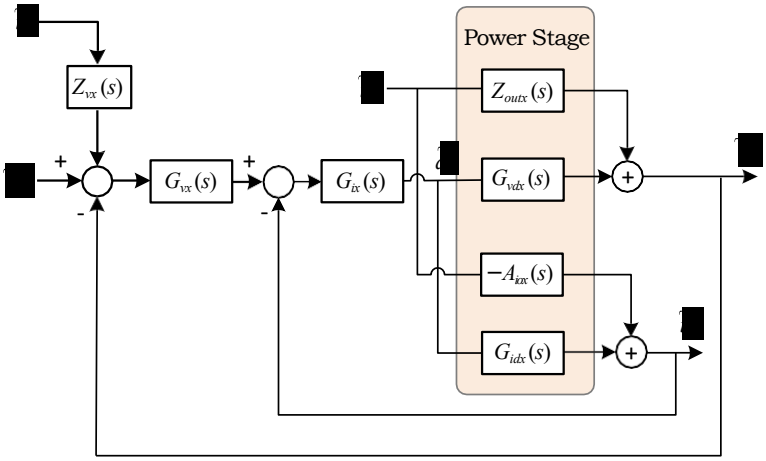


Figure 4: Small-signal control diagram of the BESS and SC converter.

respectively. The bandwidth of the current and voltage loops are designed at 2 kHz an 0.2 kHz, respectively. Furthermore, the voltage and current controllers are designed to maintain a phase margin (PM) of 60 degrees at the no-load condition. The closed-loop transfer function of Fig. 4 is derived as in (20) to verify the control system performance.

$$T_{cl}(s) = \frac{G_{vx}(s)G_{ix}(s)G_{vdx}(s)}{1 + G_{vx}(s)G_{ix}(s)G_{vdx}(s) + G_{ix}(s)G_{idx}(s)} \tag{20}$$

The closed-loop poles and zeros of (20) depicted in Fig. 5 verifies a high damping ratio and stability margin in both charging and discharging conditions. The SC voltage controller maintains the same dynamics at the no-load condition, which is the only viable linearization point since the SC maintains a zero steady-state current.

### *2.3.2. SG control*

A full-order SG model in the rotor reference frame, incorporating the dynamics of the rotor, stator and two damping windings, is considered in this study. The SG parameters can be found in [29]. The six-pulse rectifier interfacing the SG with the DC bus is modeled with a parametric average-value model [30].

A similar cascade control is implemented for the SG, representing the automatic voltage regulator (AVR) function. AC sweep is then utilized to derive small-signal transfer functions of the SG-rectifier unit, which are used

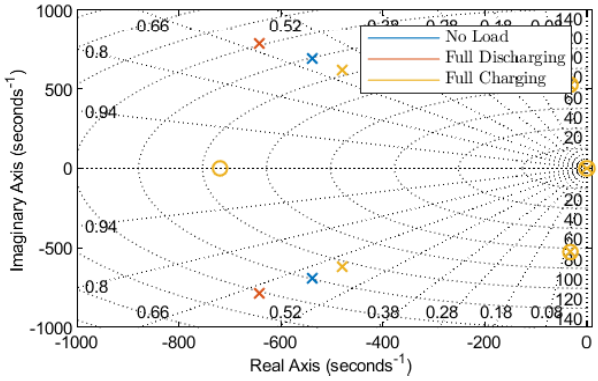


Figure 5: Pole-zero map of the BESS closed voltage loop.

to design the controllers gains of the SG. Fig. 6 shows the open-loop dynamics of the AVR at 75% loading of the SG, exhibiting a gain margin (GM) of 28 dB and a PM of 86 degrees. The robustness of the AVR is guaranteed since the variations of the SG operating point is limited to a small range above 60% of its nominal power. The voltage reference for the AVR is decided by the droop control with a gain determined by

$$R_{vsg} = \frac{\Delta V_{osgmax}}{I_{osgmax} - I_{osgmin}} \tag{21}$$

where $\Delta V_{osgmax}$ is the maximum permissible variation of the SG output voltage at steady-state, $I_{osgmax}$ is the output current rating of the SG, and $I_{osgmin}$ is the current corresponding to 60% of the SG nominal power.

The exciter is also modeled as a first-order transfer function with the generator operating under a fixed speed.

### *2.3.3. CPL control*

A buck converter tightly regulating a resistive load at 3 kV represents the CPL as the dominant load type in DC MGs. The small-signal input impedance of a 27.1 MW CPL is shown in Fig. 7. It can be seen that up to the CPL control bandwidth (200 Hz), the point-of-load converter exhibits a negative resistance behavior as the impedance phase remains close to -180 degrees. This negative small-signal resistance behavior is a well-known source of stability deterioration [31].

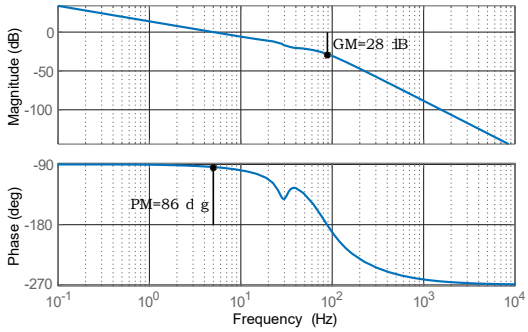


Figure 6: Bode plot of the SG open voltage loop at its 75% loading.

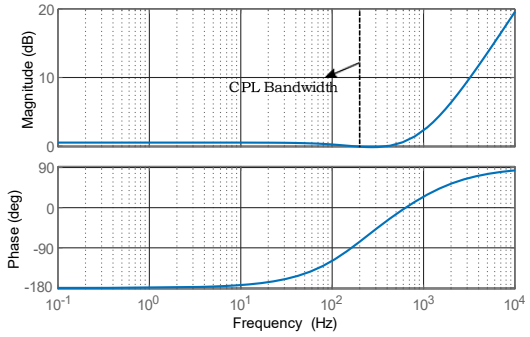


Figure 7: Input impedance of a 27.1 MW CPL.

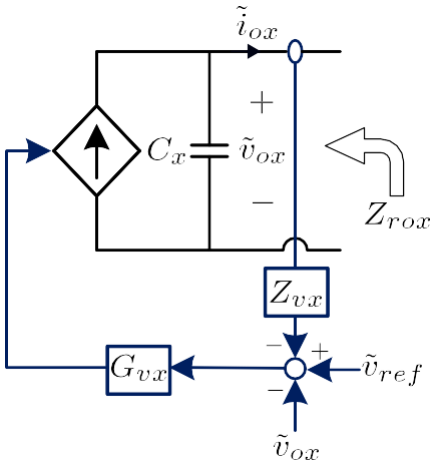


Figure 8: Small-signal reduced-order model of voltage control units.

## 3. CDC Design and Dynamic Power Sharing Analysis

In this section, the design of proposed CDC is discussed to achieve dynamic power management between the SG, BESS, and SC according to desired splitting frequencies. To do so, small-signal impedance analysis is utilized. However, it should be noted that the impedance models of the equivalent circuit in Fig. 3 are valid only at very low frequencies due to neglecting the dynamics of inner control loops and converter power stage. Therefore, to improve on the simplified impedance models and avoid dealing with detailed high-order impedances, the voltage control units inside the hybrid DC MG are modeled with the reduced-order model depicted in Fig. 8. In Fig. 8, it is assumed that the inner current loop is much faster than the outer voltage loop, and thus the converter can be modeled as a controlled current source before its output capacitor. The small-signal reduced-order output impedance of the voltage control units, $Z_{rox}(s)$, can then be obtained from Fig. 8 as

$$Z_{rox}(s) = \frac{-\tilde{v}_{ox}}{\tilde{i}_{ox}}\Big|_{\tilde{v}_{ref}=0} = \frac{1 + G_{vx}(s)Z_{vx}(s)}{G_{vx}(s) + C_x s} \tag{22}$$

where $x \in \{b, sc, sg\}$.

The reduced-order model of the hybrid DC MG model can also be illustrated as in Fig. 9. From Fig. 9, the equivalent series impedance of each

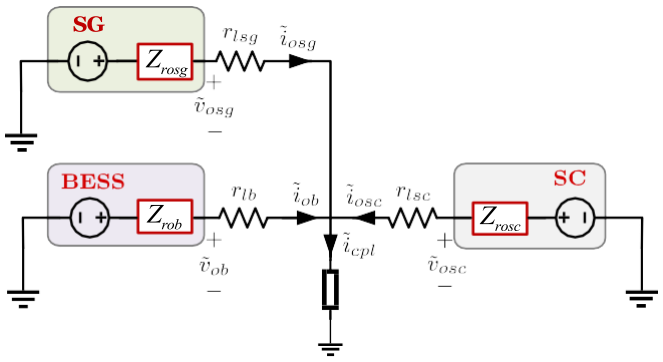


Figure 9: Small-signal reduced-order model of the hybrid DC MG.

voltage control unit is derived as $Z_{eqx} = Z_{rox} + r_{lx}$. $Z_{eqsg}$, $Z_{eqb}$, and $Z_{eqsc}$ can be compared against each other to analyze dynamic power sharing. To implement the proposed power management strategy described in Section 2.2, the following design procedure is proposed: 1) specify the splitting frequencies, i.e., $f_l$ and $f_h$, which break the frequency domain into three parts for the purpose of dynamic power sharing. $f_l$ and $f_h$ should fall within the bandwidth of AVR and BESS voltage loop, respectively [26, 32], 2) since at higher frequencies $C_x$ is the dominant term in $Z_{eqx}$, the output capacitances should be selected such that $C_{sg} < C_b < C_{sc}$, prioritizing the SC to pick up frequencies above $f_h$. 3) $|Z_{eqsg}(j\omega)|_{\omega=2\pi f_l} = |Z_{eqb}(j\omega)|_{\omega=2\pi f_l}$ is solved for $C_{vb}$, then $|Z_{eqb}(j\omega)|_{\omega=2\pi f_h} = |Z_{eqsc}(j\omega)|_{\omega=2\pi f_h}$ is solved for $C_{vsc}$.

Following the above-mentioned procedure, $f_l$ is chosen as 0.11 Hz and $f_h$ is set to 2.5 Hz, which result in $C_{vb}\approx 20$ F and $C_{vsc}\approx 5$ F. Using these values, the detailed output impedances of the SG, BESS, and SC are derived and compared in order to validate the proposed design. The detailed output impedance of the BESS and SC, $Z_{ocl}$, can be obtained from the small-signal model of Fig. 4 as in (23).

$$Z_{oclx}(s) = \frac{-\tilde{v}_{ox}}{\tilde{i}_{ox}}\Big|_{\tilde{v}_{ref},\tilde{v}=0} = \frac{Z_{outx}(s)[1 + G_{ix}(s)G_{idx}(s)]}{1 + G_{ix}(s)G_{idx}(s) + G_{vx}(s)G_{ix}(s)G_{vdx}(s)} - \frac{A_{iox}(s)G_{ix}(s)G_{vdx}(s) - Z_{vx}(s)G_{vx}(s)G_{ix}(s)G_{vdx}(s)}{1 + G_{ix}(s)G_{idx}(s) + G_{vx}(s)G_{ix}(s)G_{vdx}(s)} \quad (23)$$

where $x \in \{b, sc\}$.

The AC sweep method is also used to estimate the detailed output impedance

of the SG-rectifier unit at the operating point of interest. To do so, a small sinusoidal current at a wide range of frequencies is applied to the output of the rectifier DC link as the perturbation signal. Then, by applying the Fourier transform to the ratio of the change in the output voltage ($\tilde{v}_{osg}$) to change in the reverse output current of the DC link ($-\tilde{i}_{osg}$), the small-signal output impedance of the SG is obtained [30]. Fig. 10 shows the output impedance of the BESS, SC, and SG in mode 1 of the DC MG where all sources work in the droop control mode. The virtual capacitance values for the BESS and SC are selected as 20 F and 5 F, respectively. It can be seen that the intersection frequencies of the impedances are close to the designed values for $f_l$ and $f_h$. However, following the design procedure proposed in [26], the virtual capacitance values are obtained as $C_{vb} = 1/(2\pi f_l R_{vsg})$=28.9 F and $C_{vsc} = 1/(2\pi f_h r_{db})$=6.3 F, which leads to unacceptably large errors in the splitting frequencies.

Furthermore, the SC exhibits a very large impedance below $f_l$, rendering it open circuit in steady state. On the other hand, the SG and BESS exhibit a resistive output impedance and share the steady-state load according to their steady-state droop gains below $f_l$. Between $f_l$ and $f_h$, it is the BESS that has a significantly small impedance compared to the SG and SC. This makes the BESS the dominating source of power in the mid-frequency range. Above $f_h$, the SC exhibits a smaller output impedance than the BESS and SG, leading to it being dominant at higher frequencies. The same analysis applies to the dynamic power sharing in the second operating mode of the DC MG as shown in Fig. 11, except that the SG impedance is considerably raised above the BESS and SC impedances since in this mode the SG is controlled as a constant current source with no contribution to voltage regulation. Furthermore, comparing Fig. 10 and Fig. 11, it is clear that the BESS output impedance varies slightly from the charging to discharging mode, and the SC output impedance does not vary at all since its steady-state operating point is never changed. Therefore, the proposed dynamic power sharing strategy is robust against variations of the operating point of the microgrid.

## 4. Small-signal Stability Analysis

The unterminated stability of the power converters in the hybrid DC MG is guaranteed by proper design of their controllers. However, to get insight into dynamic interactions between the system resources, it is imperative to conduct a system-level stability analysis. Assuming the terminal voltages as

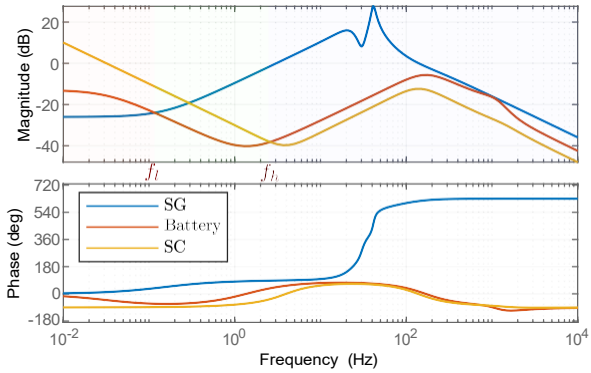


Figure 10: Output impedance of the sources in Mode 1 of the DC MG at 75% loading of the SG ($C_{vb}$=20 F, $r_{db}$=0.01 Ω, $C_{vsc}$=5 F, $r_{dsc}$=0.01 Ω).

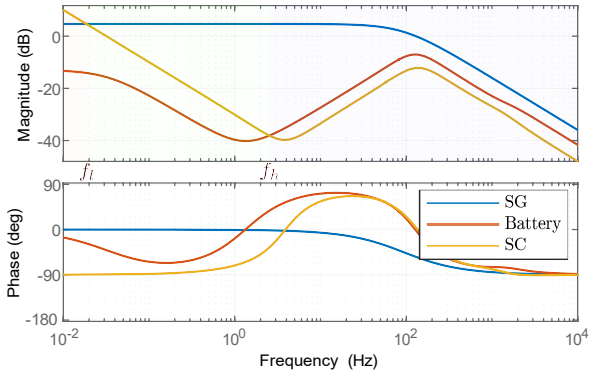


Figure 11: Output impedance of the sources in Mode 2 of the DC MG at 50% charging power of the BESS ($C_{vb}$=20 F, $r_{db}$=0.01 Ω, $C_{vsc}$=5 F, $r_{dsc}$=0.01 Ω).

the outputs of the system, and the output terminal currents as the inputs of the system, the small-signal model of (24) can be obtained for the DC MG. $Y_{sc}(s)$, $Y_b(s)$, and $Y_{sg}(s)$ are the output admittances of the SC, BESS, and SG, respectively. $Y_{lsc}(s)$, $Y_{lb}(s)$, and $Y_{lsg}(s)$ represent the line admittance of the SC, BESS, and SG, respectively. The input admittance of the load bank is represented by $Y_{load}(s)$, which consists of both the resistive load and CPL. Therefore, $\mathbf{Y_{bus}^{-1}(s)}$ is considered as the DC MG transfer function with zeros of the admittance matrix, $\mathbf{Y_{bus}}$, representing the system eigenvalues. It is found that the first and second operating modes of the system are no different in terms of dynamic response. Therefore, the following sensitivity analyses are conducted for the 1st operating mode of the DC MG for the sake of brevity.

$$\begin{bmatrix} \tilde{v}_{osc}(s) \\ \tilde{v}_{ob}(s) \\ \tilde{v}_{osg}(s) \\ \tilde{v}_{bus}(s) \end{bmatrix} = \mathbf{Y_{bus}^{-1}(s)} \begin{bmatrix} \tilde{i}_{osc}(s) \\ \tilde{i}_{ob}(s) \\ \tilde{i}_{osg}(s) \\ -\tilde{i}_{cpl}(s) \end{bmatrix} \tag{24}$$

where

$$\mathbf{Y_{bus}}(s) = \begin{bmatrix} Y_{sc} + Y_{lsc} & 0 & 0 & -Y_{lsc} \\ 0 & Y_b + Y_{lb} & 0 & -Y_{lb} \\ 0 & 0 & Y_{sg} + Y_{lsg} & -Y_{lsg} \\ -Y_{lsc} & -Y_{lb} & -Y_{lsg} & Y_{load} + Y_{lsc} + Y_{lb} + Y_{lsg} \end{bmatrix} \tag{25}$$

### *4.1. Impact of $C_{vsc}$ and $C_{vb}$*

Fig. 12 shows the effect of variations in $C_{vsc}$ on the dominant low- and high-frequency modes of the system. It can be seen that with any increase in the virtual capacitance values, the damping factor (DF) of both the dominant modes is also increased. However, it is obvious that $C_{vsc}$ has more significant effect on the high-frequency mode than the low-frequency mode. The high-frequency mode is the dominant oscillatory mode in this case since it possesses a considerably lower damping ratio than the low-frequency mode.

The effect of $C_{vb}$ on the dominant modes of the DC MG is also demonstrated in Fig. 13. Both the low- and high-frequency modes are affected by variations in $C_{vb}$. As $C_{vb}$ is increased, the damping of both modes is improved. Since the low- and high-frequency modes have comparable damping ratios in this case, the low-frequency mode will dominate the response as it is closer to the imaginary axis.

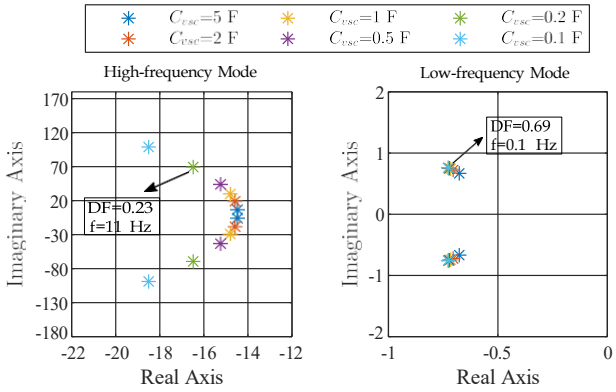


Figure 12: Effect of variations of $C_{vsc}$ on the dominant eigenvalues of the system at 75% loading of the SG ($C_{vb} = 20$, $r_{db} = 0.01$, $r_{dsc} = 0.01$, $R_{vb} = 0.225$, and $R_{vsg} = 0.05$).

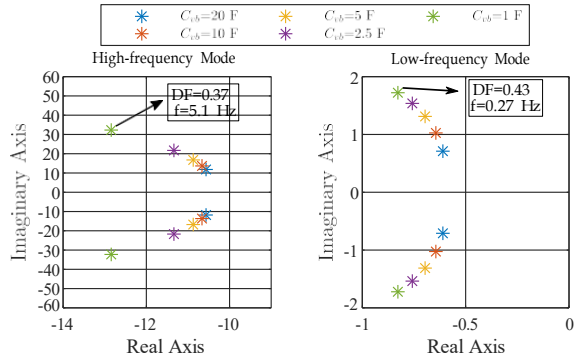


Figure 13: Effect of variations of $C_{vb}$ on the dominant eigenvalues of the system at 75% loading of the SG ($C_{vsc} = 5$, $r_{db} = 0.01$, $r_{dsc} = 0.01$, $R_{vb} = 0.225$, and $R_{vsg} = 0.05$).

### *4.2. Impact of $r_{dsc}$*

Fig. 14 shows the effect of variations in the virtual series resistance of the SC, i.e., $r_{dsc}$. It is evident from this figure that even with a small increase in $r_{dsc}$, the damping of the high-frequency mode is considerably improved. Thus, the introduction of $r_{dsc}$ to the SC control adds another degree of freedom for suppressing the dominant high-frequency mode. However, it can be seen that the low-frequency mode is not affected by $r_{dsc}$. Therefore, the high-frequency mode will be the dominant oscillatory mode since it is significantly less damped than the low-frequency mode due to the small value of $C_{vsc}$, i.e., 0.1, chosen in this particular case.

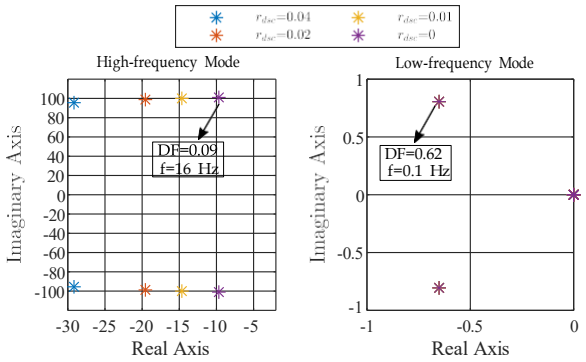


Figure 14: Effect of variations of $r_{dsc}$ on the dominant eigenvalues of the system at 75% loading of the SG ($C_{vb} = 20$, $C_{vsc} = 0.1$, $r_{db} = 0.01$, $R_{vb} = 0.225$, and $R_{vsg} = 0.05$).

### *4.3. Plug-and-Play Stability*

To evaluate the plug-and-play capability of the hybrid DC MG, the effect of various mixes of energy resources under the proposed control is investigated in this section. Following the same approach described at the beginning of Section 4, the eigenvalues of the system are derived from the admittance matrix under various mixes of energy resources and are plotted in Fig. 15. It can be seen that the DC MG remains stable under different hybridization scenarios as well as the case with a single BESS supplying the load. However, when the SG is supplying the load alone, the system becomes unstable as the dominant eigenvalues move to the right half-plane. This is due to the limited bandwidth of the SG that renders it unable to cope with the high-bandwidth CPL [33].

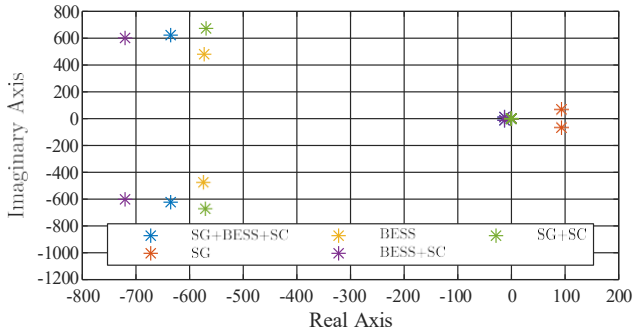


Figure 15: Dominant eigenvalues of the system under various mixes of energy resources.

## 5. Scalability Analysis

The scaled version of the hybrid DC MG with multiple sources of each type is demonstrated in Fig. 16. The equivalent impedance of $M$ parallel SGs, $N$ parallel BESSs, and $K$ parallel SCs can be represented by

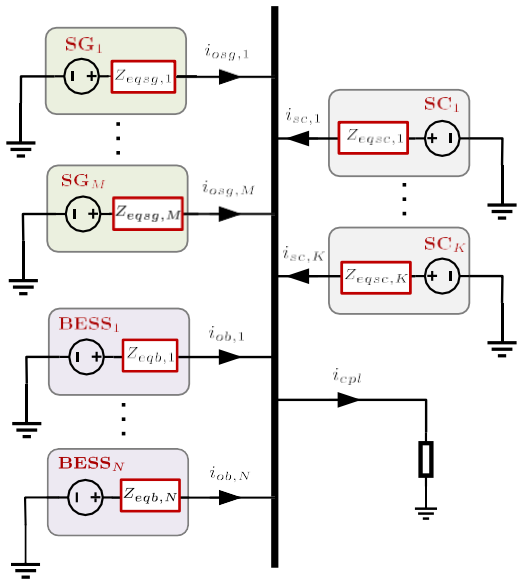


Figure 16: Scaled hybrid DC MG with multiple parallel sources.

$$\frac{1}{Z_{eqsg,T}(s)} = \sum_{m=1}^{M} \frac{1}{Z_{eqsg,m}(s)} \tag{26}$$

$$\frac{1}{Z_{eqb,T}(s)} = \sum_{n=1}^{N} \frac{1}{Z_{eqb,n}(s)} \tag{27}$$

$$\frac{1}{Z_{eqsc,T}(s)} = \sum_{k=1}^{K} \frac{1}{Z_{eqsc,k}(s)} \tag{28}$$

where $Z_{eqsg,T}(s)$, $Z_{eqb,T}(s)$, and $Z_{eqsc,T}(s)$ represent the equivalent impedances of the parallel SGs, BESSs, and SCs, respectively; $Z_{eqsg,m}(s)$, $Z_{eqb,n}(s)$, and $Z_{eqsc,k}(s)$ denote the impedances of the $m$th SG, $n$th BESS, and $k$th SC, respectively.

Let us consider the system expansion by the addition of $(M+1)^{th}$ SG, $(N+1)^{th}$ BESS, and $(K+1)^{th}$ SC. $R_{vb,(N+1)}$ and $R_{vsg,(M+1)}$ should be decided according to (12) and (21), respectively. This will ensure proportional steady-state current sharing between SGs and BESSs of various capacities as

$$I_{osg,1} : I_{osg,2} : \cdots : I_{osg,(M+1)} \propto \frac{1}{R_{vsg,1}} : \frac{1}{R_{vsg,2}} : \cdots : \frac{1}{R_{vsg,(M+1)}} \tag{29}$$

$$I_{ob,1} : I_{ob,2} : \cdots : I_{ob,(N+1)} \propto \frac{1}{R_{vb,1}} : \frac{1}{R_{vb,2}} : \cdots : \frac{1}{R_{vb,(N+1)}} \tag{30}$$

where $I_{osg,m}$ and $I_{ob,n}$ denote the steady-state output current of $m$th SG and $n$th BESS, respectively.

In order to maintain the splitting frequency between the SGs and BESSs at $f_l$, the following equation is solved for $C_{vb,(N+1)}$.

$$\left| \frac{Z_{eqsg,T}(j\omega) Z_{eqsg,(M+1)}(j\omega)}{Z_{eqsg,T}(j\omega) + Z_{eqsg,(M+1)}(j\omega)} \right|_{\omega=2\pi f_l} = \left| \frac{Z_{eqb,T}(j\omega) Z_{eqb,(N+1)}(j\omega)}{Z_{eqb,T}(j\omega) + Z_{eqb,(N+1)}(j\omega)} \right|_{\omega=2\pi f_l} \tag{31}$$

After finding $C_{vb,(N+1)}$ using the above equation, the equivalent impedance of the $(N+1)$ BESSs is set equal to the equivalent impedance of the $(K+1)$ SCs to solve for $C_{sc,(K+1)}$ as follows.

$$\left| \frac{Z_{eqb,T}(j\omega) Z_{eqb,(N+1)}(j\omega)}{Z_{eqb,T}(j\omega) + Z_{eqb,(N+1)}(j\omega)} \right|_{\omega=2\pi f_h} = \left| \frac{Z_{eqsc,T}(j\omega) Z_{eqsc,(K+1)}(j\omega)}{Z_{eqsc,T}(j\omega) + Z_{eqsc,(K+1)}(j\omega)} \right|_{\omega=2\pi f_h} \tag{32}$$

The $C_{sc,(K+1)}$ obtained from the equation above will guarantee the splitting frequency between the BESSs and SCs at $f_h$.

The transient current sharing between the individual BESSs and SCs will then follow

$$\tilde{i}_{ob,1} : \tilde{i}_{ob,2} : \cdots : \tilde{i}_{ob,(N+1)} \propto C_{vb,1} : C_{vb,2} : \cdots : C_{vb,(N+1)} \tag{33}$$

$$\tilde{i}_{osc,1} : \tilde{i}_{osc,2} : \cdots : \tilde{i}_{osc,(K+1)} \propto C_{vsc,1} : C_{vsc,2} : \cdots : C_{vsc,(K+1)} \tag{34}$$

where $\tilde{i}_{ob,n}$ and $\tilde{i}_{osc,k}$ denote the transient output current of $n$th SG and $k$th BESS, respectively.

Table 3: Hybrid DC MG simulation parameters

| Parameter | Value |
|---|---|
| $C_{sg}$, $C_b$, $C_{sc}$, $C_{cpl}$ | 1 mF, 2 mF, 4 mF, 27 $\mu$F |
| $L_b$, $L_{sc}$, $L_{cpl}$ | 0.8 mH, 0.8 mH, 56 $\mu$H |
| $r_{Lb}$, $r_{Lsc}$, $r_{Lcpl}$ | 0.05 Ω |
| $r_{lsg}$, $r_{lb}$, $r_{lsc}$ | 0.4 mΩ |
| $\upsilon_{ref}$, $\upsilon_{lref}$ | 6 kV, 3 kV |
| $\omega_r$ | 1800 rpm |
| $R_{\upsilon sg}$, $R_{\upsilon b}$ | 0.05 Ω, 0.225 Ω |
| $G_{\upsilon sg}$, $G_{isg}$ | 0.02+18.9/s, 8.2+45.1/s |
| $G_{\upsilon b}$, $G_{ib}$ | 3.4+1790/s, 0.001+10.6/s |
| $G_{\upsilon sc}$, $G_{isc}$ | 6.4+4620/s, 0.001+10.6/s |
| CPL voltage controller | 0.22/s |

## 6. Simulation results

Simulation case studies are conducted in Simulink® using the Simscape™ library for the hybrid DC MG of Fig. 1. In the first three case studies, a step decrease of 0.03 Ω is applied to $R_{cpl}$ at $t$=1 s, resulting in about 3.6 MW of instantaneous increase in the CPL power. The simulation parameters are given in Table 3.

### *6.1. Verification of virtual capacitance impact*

Fig. 17 demonstrates the DC MG transient behavior under various values of $C_{\upsilon sc}$. As $C_{\upsilon sc}$ is increased, the damping of the high-frequency mode is improved and the voltage overshoot is reduced as shown in Fig. 17(a). From Fig. 17(b) and Fig. 17(d), it is clear that the current stress on the BESS and SG is also reduced with larger values of $C_{\upsilon sc}$. However, a larger $C_{\upsilon sc}$ leads to an increased time constant for the SC and more energy drawn from it according to Fig. 17(c). The results are in line with the sensitivity analysis in Fig. 12 as the oscillation period of the high-frequency mode agrees with the the frequency in Fig. 12.

The effect of various $C_{\upsilon b}$ values is investigated in Fig. 18. Larger values of $C_{\upsilon b}$ evidently contribute to the damping enhancement of low- and high-frequency oscillations. However, a larger $C_{\upsilon b}$ also leads to a higher surge

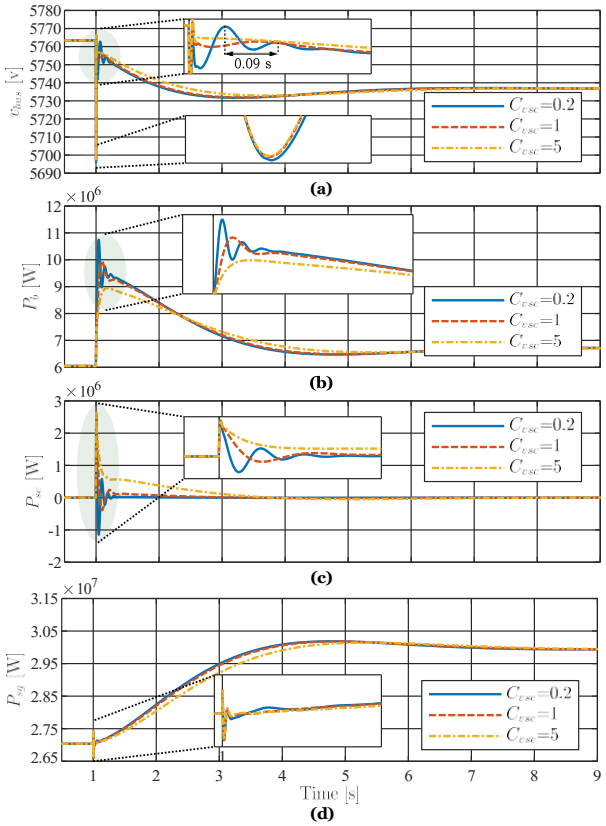


Figure 17: Transient response of (a) DC bus voltage, (b) BESS power, (c) SC power, and (d) SG power, subject to a pulsed load change and various values of $C_{vsc}$ ($C_{vb}$=20 F, $r_{db}$=0.01 Ω, $r_{dsc}$=0.01 Ω).

power from the BESS according to Fig. 18(b), which calls for the oversizing of the BESS. It can also be seen that the voltage undershoot remains unchanged since $C_{vb}$ does not affect the surge power provided by the SC. Comparing the low-frequency oscillation period in Fig. 18(a) with the mode's frequency in Fig. 13, simulation results are found to be consistent with the stability analysis findings.

### 6.2. *Verification of $r_{dsc}$ impact*

Previously, it was shown that increasing the virtual capacitance values ($C_{vsc}$ and $C_{vb}$) contributes to the damping of high-frequency oscillations in the hybrid DC MG. However, increasing the virtual capacitance values results in higher transient power from the BESS and SC, and thus requires

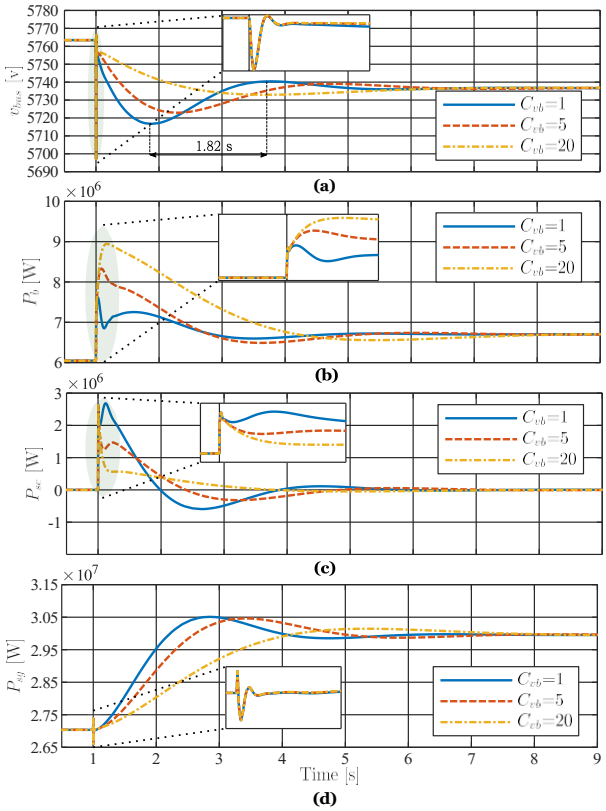


Figure 18: Transient response of (a) DC bus voltage, (b) BESS power, (c) SC power, and (d) SG power, subject to a pulsed load change and various values of $C_{vb}$ ($C_{vsc}$=5 F, $r_{db}$=0.01 Ω, $r_{dsc}$=0.01 Ω).

them to be oversized. Fig. 19 illustrates how different values of $r_{dsc}$ affect the high-frequency mode as the system is subjected to the pulsed load at $t$=1 s. It can be seen that with even a small increase in $r_{dsc}$, the damping of the dominant high-frequency mode is considerably improved while the low-frequency damping is not affected. However, a larger $r_{dsc}$ also results in reduced surge power for the SC and thus a larger undershoot according to Fig. 19(a). Therefore, a small value of virtual resistance for the SC is recommended to improve the high-frequency damping and prevent the oversizing of the BESS and SC for damping purposes. The results are in agreement with the stability analysis of Fig. 14 as the high-frequency oscillation period agrees with the frequency of the mode.

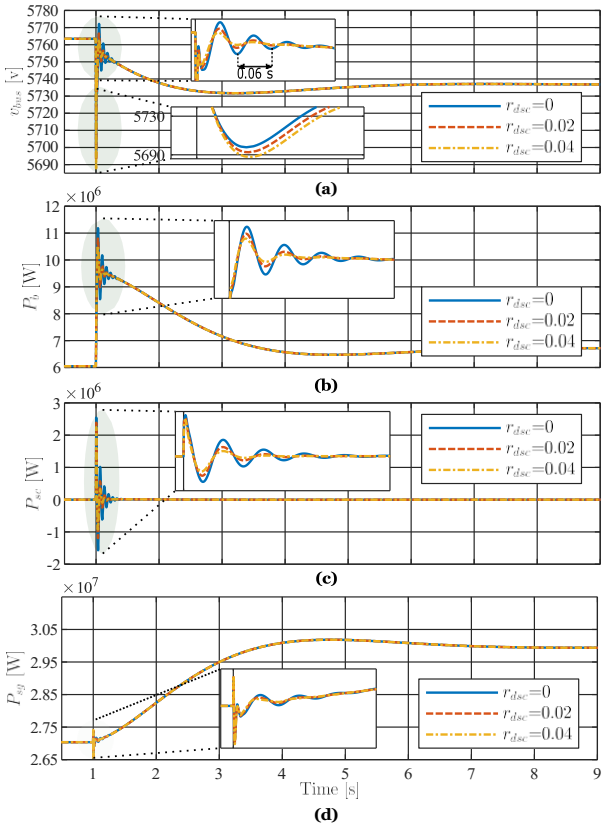


Figure 19: Transient response of (a) DC bus voltage, (b) BESS power, (c) SC power, and (d) SG power, subject to a pulsed load change and various values of $r_{dsc}$ ($C_{vb}$=20 F, $C_{vsc}$=0.1 F, $r_{db}$=0.01 Ω).

### *6.3. Plug-and-play performance*

The plug-and-play performance is evaluated by a case study where the SG, BESS are supplying the load, and the SC is in the idle mode due to the system being at steady state. Two contingency scenarios are applied to the DC MG at t=1 s as can be seen in Fig. 20. In one of them, the SG and SC are disconnected at the same time and in the other one the BESS and SC are disconnected. It can be noticed that the system goes unstable as soon as the BESS and SC are plugged out. However, the stability is maintained when the SG and SC are disconnected as the BESS continues to supply the load alone. This is in line with the analysis provided in Section. 4.3, where it was shown that the low bandwidth of the SG renders it unable to supply

the tightly-regulated CPL alone.

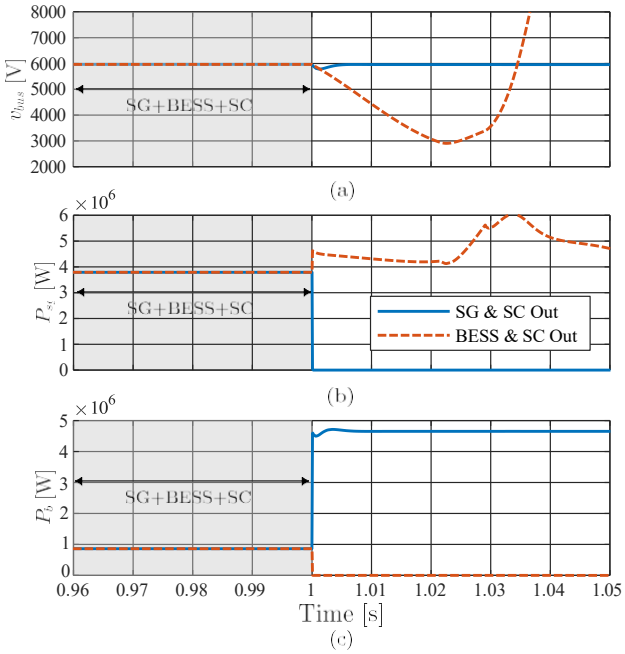


Figure 20: Plug-and-play performance verification of the hybrid DC MG.

### *6.4. Power sharing between homogeneous sources*

In this case study, the power sharing between homogeneous sources of the hybrid DC MG is investigated. To do so, two parallel SGs, BESSs, and SCs are considered with droop gains defined as $R_{vsg,1} = 0.05\ \Omega$, $R_{vsg,2} = 0.1\ \Omega$, $R_{vb,1} = 0.225\ \Omega$, $R_{vb,2} = 0.45\ \Omega$, $C_{vb,1} = 20\ F$, $C_{vb,2} = 40\ F$, $C_{vsc,1} = 5\ F$, $C_{vsc,2} = 10\ F$.

Fig. 21 depicts the power sharing performance as a 7 MW step increase in the CPL is applied at t=2 s. The steady-state powers of SG1 and BESS1 are twice those of SG2 and BESS2, respectively. This is because the steady-state power is inversely proportional to droop gains $R_{vsg}$ and $R_{vb}$. On the other hand, BESS2 and SC2 provide more transient power since their transient powers are proportional to $C_{vb}$ and $C_{sc}$, respectively. This is consistent with the scalability analysis provided in Section 5, where it was shown that any increase in the virtual capacitance will lead to a higher share of transient power.

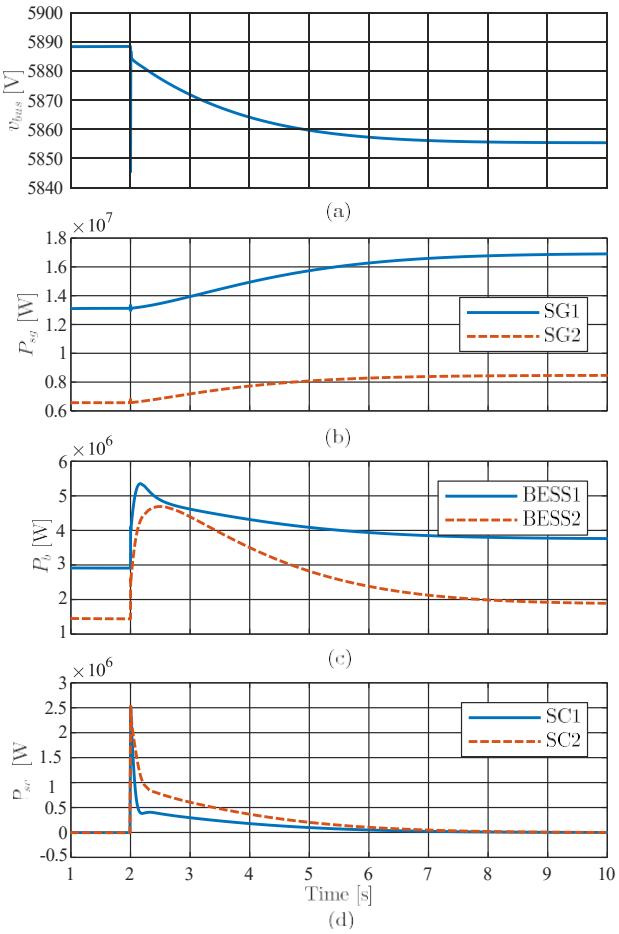


Figure 21: Power sharing between homogeneous sources of the hybrid DC MG.

### *6.5. Comparison case study*

A direct comparison between the proposed CDC and the virtual resistive capacitive droop (VRCD) of [26] is conducted in Fig. 22, where a pulsed load of 7 MW is applied at t=2 s. In both methods, dynamic power sharing is realized between the system sources as the SG responds to the low-frequency component of the power disturbance, while the BESS and SC tackle the medium- and high-frequency components of the power, respectively. However, the transient responses differ due to different droop parameters. As discussed in Section 3, the proposed method is more truthful to the desired splitting frequencies.

Furthermore, it can be noticed in Fig. 22(c) that the BESS does not

contribute to the steady-state voltage regulation when the VRCD is used, whereas with the CDC, the BESS provides back-up power in steady-state in addition to addressing the medium-frequency disturbance. With two parallel droop-controlled sources contributing to the steady-sate voltage regulation, the equivalent steady-state droop gain drops from $R_{vsg} = 0.05\ \Omega$ to $\frac{R_{vsg}R_{vb}}{R_{vsg}+R_{vb}} = 0.0418\ \Omega$, resulting in less voltage drop as shown in Fig. 22(a) in addition to reduction in the SG required power shown in Fig. 22(b).

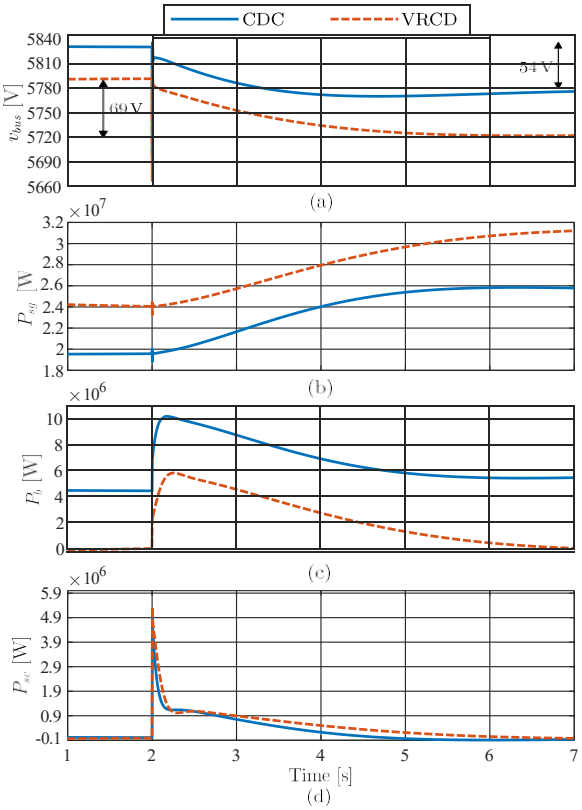


Figure 22: Transient response of (a) DC bus voltage, (b) SG power, (c) BESS power, and (d) sources power in the method of [26], subject to a 7 MW pulsed load change.

## *6.6. Experimental Verification*

The comparison case study of Section 6.5 is replicated using the OPAL-RT real-time simulation setup shown in Fig. 23. To this end, first the hybrid DC MG of Fig. 1 is built in Simulink® and compiled in RT-LAB. The model is then executed on one of the CPU cores of the OP4510 real-time target and

is controlled using the Simulink® GUI on the host PC through a TCP/IP link. Desired measurements are then sent to a digital oscilloscope in real-time via the analog outputs of OP4510 target.

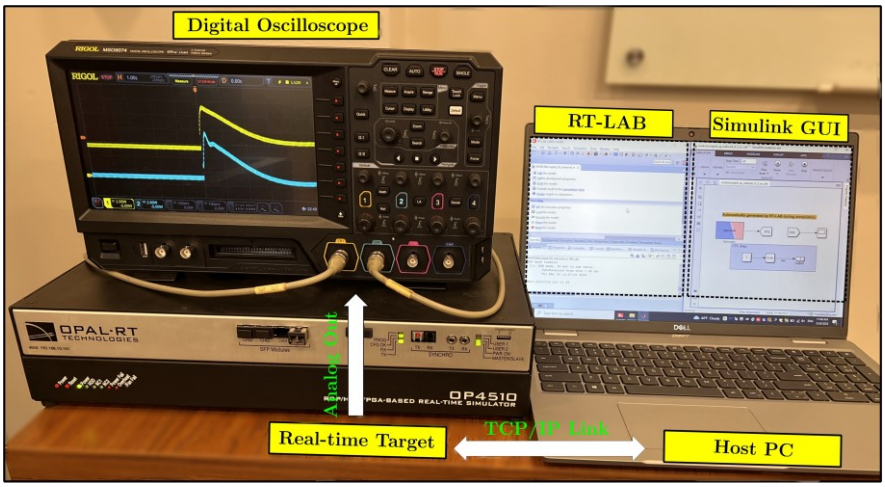


Figure 23: Real-time simulation testbed.

As can be seen from Fig. 24, the CDC method results in improved voltage regulation and reduced SG backup power when compared with the VRCD method. Furthermore, the improved damping of the CDC scheme can be testified from the BESS and SC power profiles during the transient event.

## 7. Discussion & Conclusion

In this research, a CDC scheme is proposed for the power management of a hybrid DC MG. The proposed CDC is capable of providing multiple functions such as adjusting the steady-state and dynamic power sharing between heterogeneous sources over the entire frequency range while providing damping function. A detailed design procedure for the CDC is proposed, which leverages a reduced-order model of the DC MG and improves on the existing simplified models that lead to large errors in the DC MG splitting frequencies governing the dynamic power sharing behavior. Furthermore, a comprehensive small-signal modeling of the hybrid DC MG reveals two dominant modes of low and high frequency and the potential of the proposed control in damping enhancement of the high-frequency mode, preventing the need for oversized BESS and SC. The results of the study provide design guidelines for droop-based dynamic power management in hybrid DC MGs.

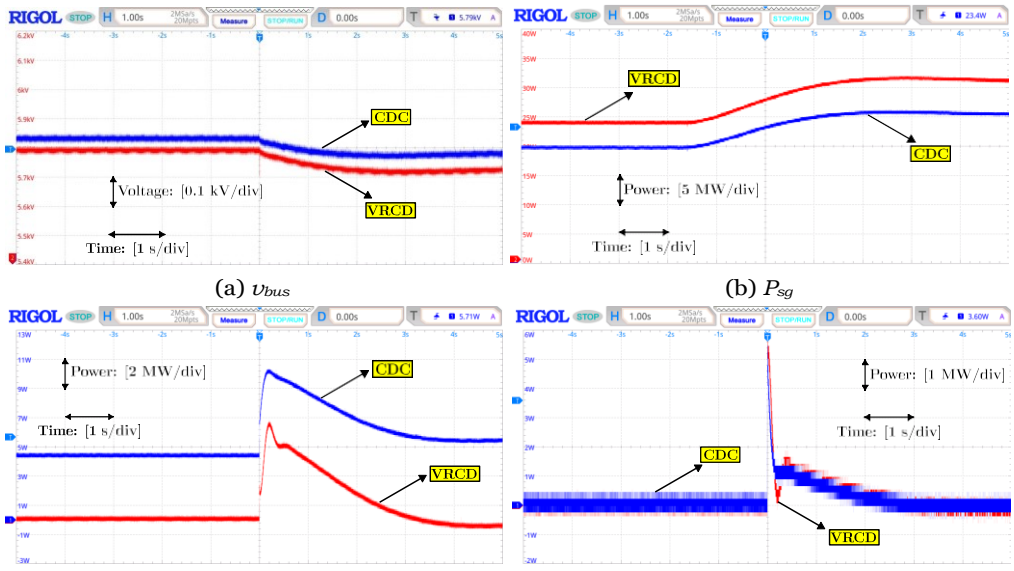


(a) $v_{bus}$ (b) $P_{sg}$

(c) $P_b$ (d) $P_{sc}$

Figure 24: Real-time verification of the proposed CDC against VRCD.

## References


[1] X. Zhu, H. Hu, H. Tao, Z. He, Stability analysis of pv plant-tied mvdc railway electrification system, IEEE Transactions on Transportation Electrification 5 (1) (2019) 311–323. doi:10.1109/TTE.2019.2900857.

[2] N. Zohrabi, J. Shi, S. Abdelwahed, An overview of design specifications and requirements for the mvdc shipboard power system, Int J. Electr. Power Energy Syst. 104 (2019) 680–693. doi:https://doi.org/10.1016/j.ijepes.2018.07.050.

[3] I. Alhurayyis, A. Elkhateb, D. J. Morrow, Bidirectional dc-dc resonant converter design for electric vehicle charging stations integration to mvdc grids, in: 2020 9th International Conference on Renewable Energy Research and Application (ICRERA), 2020, pp. 236–241. doi:10.1109/ICRERA49962.2020.9242656.

[4] J. K. Steinke, P. Maibach, G. Ortiz, F. Canales, P. Steimer, Mvdc applications and technology, in: PCIM Europe 2019; International Exhibition and Conference for Power Electronics, Intelligent Motion, Renewable Energy and Energy Management, 2019, pp. 1–8.

[5] Z. Jin, G. Sulligoi, R. Cuzner, L. Meng, J. C. Vasquez, J. M. Guerrero, Next-generation shipboard dc power system: Introduction smart grid and dc microgrid technologies into maritime electrical netowrks, IEEE Electrific. Mag. 4 (2) (2016) 45–57. doi:10.1109/MELE.2016.2544203.

[6] A. Kaysal, S. Köroğlu, Y. Oğuz, Hierarchical energy management system with multiple operation modes for hybrid dc microgrid, Int J. Electr. Power Energy Syst. 141 (2022) 108149. doi:https://doi.org/10.1016/j.ijepes.2022.108149.

[7] M. B. Othman, N. P. Reddy, P. Ghimire, M. K. Zadeh, A. Anvari-Moghaddam, J. M. Guerrero, A hybrid power system laboratory: Testing electric and hybrid propulsion, IEEE Electrific. Mag. 7 (4) (2019) 89–97. doi:10.1109/MELE.2019.2943982.

[8] L. Xu, B. Wei, Y. Yu, J. M. Guerrero, J. Vasquez, Coordinated control of diesel generators and batteries in dc hybrid electric shipboard power system, Energies 14 (19) (2021). doi:10.3390/en14196246.
URL https://www.mdpi.com/1996-1073/14/19/6246

[9] M. U. Mutarraf, Y. Terriche, M. Nasir, Y. Guan, C.-L. Su, J. C. Vasquez, J. M. Guerrero, A communication-less multimode control approach for adaptive power sharing in ship-based seaport microgrid, IEEE Trans. Transport. Electrific. 7 (4) (2021) 3070–3082. doi:10.1109/TTE.2021.3087722.

[10] P. Ghimire, M. Zadeh, E. Pedersen, J. Thorstensen, Dynamic modeling, simulation, and testing of a marine dc hybrid power system, IEEE Trans. Transport. Electrific. 7 (2) (2021) 905–919. doi:10.1109/TTE.2020.3023896.

[11] L. W. Y. Chua, T. Tjahjowidodo, G. G. L. Seet, R. Chan, Implementation of optimization-based power management for all-electric hybrid vessels, IEEE Access 6 (2018) 74339–74354. doi:10.1109/ACCESS.2018.2883324.

[12] C. S. Edrington, G. Ozkan, B. Papari, D. E. Gonsoulin, D. Perkins, T. V. Vu, H. Vahedi, Distributed energy management for ship power systems with distributed energy storage, J. Mar. Eng. Technol. 19 (sup1) (2020) 31–44. doi:10.1080/20464177.2019.1684122.

[13] C. S. Edrington, G. Ozkan, B. Papari, D. Perkins, Distributed adaptive power management for medium voltage ship power systems, J. Mar. Eng. Technol. 0 (0) (2021) 1–16. arXiv:https://doi.org/10.1080/20464177.2021.1894783, doi:10.1080/20464177.2021.1894783.
URL https://doi.org/10.1080/20464177.2021.1894783

[14] H. Shayeghi, F. Monfaredi, A. Dejamkhooy, M. Shafie-khah, J. Catalão, Assessing hybrid supercapacitor-battery energy storage for active power management in a wind-diesel system, Int J. Electr. Power Energy Syst. 125 (2021) 106391. doi:https://doi.org/10.1016/j.ijepes.2020.106391.

[15] Z. Jin, L. Meng, J. M. Guerrero, R. Han, Hierarchical control design for a shipboard power system with dc distribution and energy storage aboard future more-electric ships, IEEE Trans. Ind. Informat. 14 (2) (2018) 703–714. doi:10.1109/TII.2017.2772343.

[16] Z.-X. Xiao, H.-M. Li, H.-W. Fang, Y.-Z. Guan, T. Liu, L. Hou, J. M. Guerrero, Operation control for improving energy efficiency of shipboard microgrid including bow thrusters and hybrid energy storages, IEEE Trans. Transport. Electrific. 6 (2) (2020) 856–868. doi:10.1109/TTE.2020.2992735.

[17] R. F. Bastos, C. R. Aguiar, A. Balogh, Z. Sütő, R. Q. Machado, Power-sharing for dc microgrid with composite storage devices and voltage restoration without communication, Int J. Electr. Power Energy Syst. 138 (2022) 107928. doi:https://doi.org/10.1016/j.ijepes.2021.107928.

[18] Y. Zhang, Y. Wei Li, Energy management strategy for supercapacitor in droop-controlled dc microgrid using virtual impedance, IEEE Trans. Power Electron. 32 (4) (2017) 2704–2716. doi:10.1109/TPEL.2016.2571308.

[19] K. Kumar, S. Bae, Dynamic power management based on model predictive control for hybrid-energy-storage-based grid-connected microgrids, Int J. Electr. Power Energy Syst. 143 (2022) 108384. doi:https://doi.org/10.1016/j.ijepes.2022.108384.

[20] F. Ni, Z. Zheng, Q. Xie, X. Xiao, Y. Zong, C. Huang, Enhancing resilience of dc microgrids with model predictive control based hybrid

energy storage system, Int J. Electr. Power Energy Syst. 128 (2021) 106738. doi:https://doi.org/10.1016/j.ijepes.2020.106738.

[21] S. A. Ghorashi Khalil Abadi, S. I. Habibi, T. Khalili, A. Bidram, A model predictive control strategy for performance improvement of hybrid energy storage systems in dc microgrids, IEEE Access 10 (2022) 25400–25421. doi:10.1109/ACCESS.2022.3155668.

[22] Q. Xu, X. Hu, P. Wang, J. Xiao, P. Tu, C. Wen, M. Y. Lee, A decentralized dynamic power sharing strategy for hybrid energy storage system in autonomous dc microgrid, IEEE Trans. Ind. Electron. 64 (7) (2017) 5930–5941. doi:10.1109/TIE.2016.2608880.

[23] P. Lin, P. Wang, J. Xiao, J. Wang, C. Jin, Y. Tang, An integral droop for transient power allocation and output impedance shaping of hybrid energy storage system in dc microgrid, IEEE Trans. Power Electron. 33 (7) (2018) 6262–6277. doi:10.1109/TPEL.2017.2741262.

[24] J. Khazaei, Optimal flow of mvdc shipboard microgrids with hybrid storage enhanced with capacitive and resistive droop controllers, IEEE Trans. Power Syst. 36 (4) (2021) 3728–3739. doi:10.1109/TPWRS.2021.3049343.

[25] Z.-X. Xiao, Y.-Z. Guan, H.-W. Fang, Y. Terriche, J. M. Guerrero, Dynamic and steady-state power-sharing control of high-efficiency dc shipboard microgrid supplied by diesel generators, IEEE Syst. J. (2021) 1–12doi:10.1109/JSYST.2021.3111685.

[26] X. Chen, J. Zhou, M. Shi, L. Yan, W. Zuo, J. Wen, A novel virtual resistor and capacitor droop control for hess in medium-voltage dc system, IEEE Trans. Power Syst. 34 (4) (2019) 2518–2527. doi:10.1109/TPWRS.2019.2894754.

[27] U. Javaid, F. D. Freijedo, D. Dujic, W. van der Merwe, Dynamic assessment of source–load interactions in marine mvdc distribution, IEEE Trans. Ind. Electron. 64 (6) (2017) 4372–4381. doi:10.1109/TIE.2017.2674597.

[28] D. W. Hart, Power Electronics, McGraw-Hill, New York, NY, USA, 2011.

[29] B. Zahedi, L. E. Norum, Modeling and simulation of all-electric ships with low-voltage dc hybrid power systems, IEEE Trans. Power Electron. 28 (10) (2013) 4525–4537. doi:10.1109/TPEL.2012.2231884.

[30] J. Jatskevich, S. Pekarek, A. Davoudi, Parametric average-value model of synchronous machine-rectifier systems, IEEE Trans. Energy Convers. 21 (1) (2006) 9–18. doi:10.1109/TEC.2005.847974.

[31] M. Pourmohammad, M. Toulabi, M. Rayati, S. A. Khajehoddin, Load type impacts on the stability and robustness of dc microgrids, Int J. Electr. Power Energy Syst. 140 (2022) 108036. doi:https://doi.org/10.1016/j.ijepes.2022.108036.

[32] L. J. Rashkin, J. C. Neely, D. G. Wilson, S. F. Glover, N. Doerry, S. Markle, T. J. McCoy, Energy storage design considerations for an mvdc power system, Journal of Marine Engineering & Technology 19 (sup1) (2020) 92–103.

[33] M. A. Bianchi, I. G. Zurbriggen, F. Paz, M. Ordonez, Improving dc microgrid dynamic performance using a fast state-plane-based source-end controller, IEEE Transactions on Power Electronics 34 (8) (2019) 8062–8078. doi:10.1109/TPEL.2018.2878383.